

A SPICE Model for a Novel Brushless Adjustable-Speed Drive

Michael A. Inerfield, *Student Member, IEEE*, Steven L. Garverick, *Senior Member, IEEE*, Wyatt S. Newman, *Member, IEEE*, and Yuandao Zhang

Abstract—A SPICE circuit model was developed to accurately simulate the i - v characteristics of a brushless ac motor commutated by semiconductor switches. The model is based on Fourier curve fits to measured mutual inductance interactions between all combinations of field and armature windings, as well as coil resistance and inductance. The model is able to accurately predict current and voltage characteristics, both statically, and dynamically when interfaced with a commutation model. The model has been demonstrated to agree with electrical tests of an inverted motor on a large time scale. It has also given reliable predictions of small time-scale details, where it is desirable to predict power MOSFET switch behavior after a command to open or close. Data were collected and analyzed for simulations of the motor model combined with a commutation model containing MOSFET switches. Metrics were compared to data collected from an inverted brushless motor with good agreement.

Index Terms—Adjustable-speed drive, commutation, modeling, SPICE.

I. INTRODUCTION

A. Background

ADJUSTABLE-SPEED drives (ASDs) from the fractional horsepower to kilohorsepower range have a variety of existing and potential applications ranging from consumer appliances and residential heating, ventilation, and air conditioning (HVAC) equipment at the fractional and low horsepower level, to commercial machinery such as textile handlers, construction equipment, gas and chemical pumps, and manufacturing robotics at higher horsepower ratings [1], [2]. In high-end applications, improvement in power efficiency justifies the cost of the complex electronics required in such a drive. Mainstream consumer and residential applications, which demand inexpensive, low-maintenance equipment, will also adopt ASD technology when the cost of electronics is reduced.

ASDs are typically implemented using solid-state electronics and have existed for more than 30 years. Electronics for dc drives that allow variable-speed operation are generally simpler and more economical than for comparable ac systems. Speed control in a dc ASD is almost always achieved by adjusting the supply voltage [1]. Simple, economical methods of adjusting the dc supply voltage include motor-generator sets, mercury-arc

rectifiers, and thyristors [1]. Unfortunately, dc drives suffer a range of problems from the carbon brushes typically used to perform commutation. Mechanical commutators have short lifetimes and require frequent maintenance. These brushes cause power loss by friction and heating, and the sparks produced make them too dangerous to use in some applications [3].

B. Brushless ASD

In this paper, we describe the analysis of a new type of brushless ac motor that has the potential for attractive price versus performance relative to existing ASDs. The motor design that is the subject of this work, introduced in [4]–[6], is a novel concept that does not fall within traditional categories of motors. We will refer to this design as the “DynaMotor,” a market name ascribed to it by DynaMotors, Inc., Cleveland, OH. Fig. 1(a) shows an axial view of a 12-coil version of the motor, illustrating connections for the power supply, armature windings, and their associated switches. Fig. 1(b) is a photograph of a prototype motor, which shows commutation control circuitry, power MOSFET switches, and a view of the armature winding geometry.

The principal advantages of this motor over a dc ASD are in its noncontact commutation and ability to be powered directly from a single-phase ac line. Avoiding the use of the expensive electronics typically found in an inverter gives it advantages over ac ASDs as well. Furthermore, inverter-based ac ASDs typically require three-phase power [7], limiting their use in residential settings. In the next section, we introduce the novel DynaMotor design, providing the background for our dynamic electromechanical model of its operation.

Structurally, the DynaMotor is similar to a universal series motor, in that rotor windings are enabled as a function of mechanical rotor angle. The new design, however, differs from the universal motor in that the rotor coils are not directly excited by a power source, and that there are no mechanical brushes or slip rings. Instead, shorted rotor coils are excited inductively by mutual inductance with respect to the powered stator coil(s). This feature of the new design is closely related to the operation of an induction motor. However, an induction motor conventionally has all rotor windings permanently shorted, typically via solid bars interconnected in a squirrel-cage configuration. In contrast, the DynaMotor has wound, isolated rotor coils that can be selectively shorted by power semiconductors. Commutation instructions are wirelessly transmitted from the field to the armatures by means such as through inductively coupled coils [8].

The experimental prototype DynaMotor was fabricated by removing the mechanical commutator from a universal series

Manuscript received March 11, 1999; revised May 27, 2000. Abstract published on the Internet September 6, 2000. This work was supported by the the Cleveland Advanced Manufacturing Program (CAMP) and DynaMotors, Inc.

The authors are with the Department of Electrical Engineering and Computer Science, Case Western Reserve University, Cleveland, OH 44106 USA (e-mail: mai3@po.cwru.edu).

Publisher Item Identifier S 0278-0046(00)10268-0.

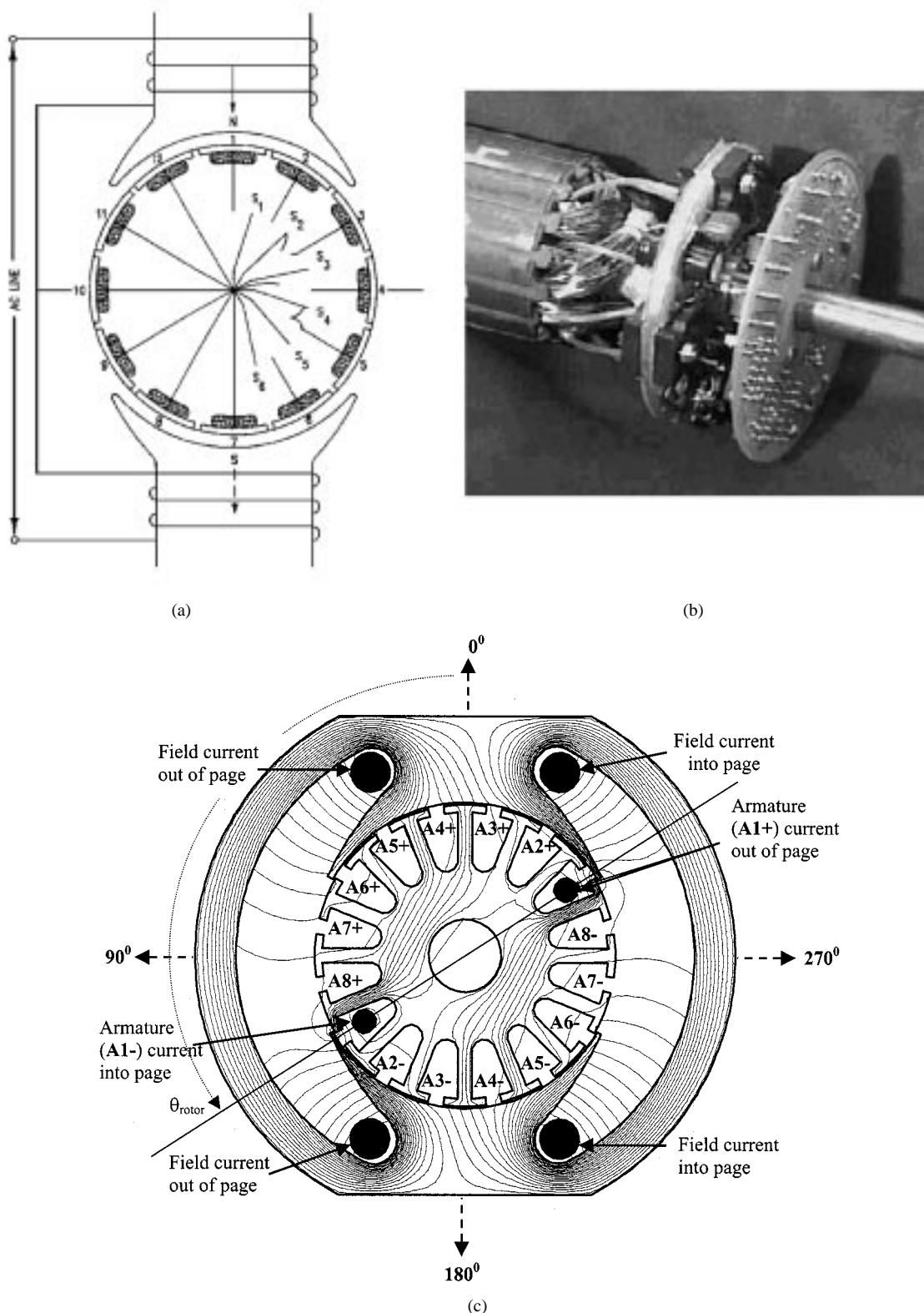


Fig. 1. (a) Schematic axial view of brushless adjustable-speed motor (based upon U.S. Patent 5 424 625). (b) Prototype brushless adjustable-speed motor. The circuit board on the right contains switching logic and wireless communication circuitry. The left circuit board contains power MOSFET switches and wireless communication circuitry. (c) Cross section of the motor and finite-element solution for magnetic flux for excitation of the field (+319 A-t) and response of shorted armature coil 1 (–170 A-t).

motor and replacing this function with electronics. In the original universal motor design, the stator coil and rotor coils conformed to the conventional definitions of a field winding and armature windings, respectively. In the prototype, we continue

to use the terms field and armature ascribed to the original universal design, since “rotor” and “stator” are reversed in our test apparatus. For convenience of data collection, the experimental apparatus was “inverted” in the sense that the armature (nor-

mally the rotor) was held fixed, while the field (normally the stator) was allowed to rotate. The field winding in this apparatus was connected to ac power via slip rings, while the stationary armature windings were extended out so that direct measurements of the (normally hidden) states could be obtained.

The principal of operation of the DynaMotor is illustrated in the cross-sectional view of Fig. 1(c), which shows a finite-element solution of the magnetic field distribution and illustrates the field and armature coil geometry. Armature coil current is induced in response to a changing field current, since a shorted armature coil behaves equivalently to a shorted secondary of a transformer. Heuristically, the current response in a shorted armature coil acts to prevent a change of flux linkage with respect to the shorted coil, as is apparent from the flux lines in Fig. 1(c).

In our test apparatus, eight isolated armature coils were wound in diametrically opposed slot pairs. In Fig. 1(c), armature coil 1 is threaded axially into slot A1+, connecting 180° about the rotor to slot A1−, and returning axially out of slot A1−, back to slot A1+. Each coil is interrupted by a semiconductor switch, which makes the respective coil behave as though it is either directly shorted or open circuited, depending on the state of the switch. All eight armature coils were wound in a similar manner. Each coil's switch could be open or short circuited under computer control.

For armatures in the range of 0°–90° in Fig. 1(c), a negative torque is produced, acting to accelerate the armature in a clockwise direction (or the field in a counterclockwise direction, in our inverted test apparatus). This torque may be visualized equivalently in terms of the Maxwell stress tensor (due to the curvature of the field lines in the air gap), in terms of variable reluctance (visualizing the action of flux shielding as an equivalent change in active cross-sectional area of the flux bundles crossing the air gap), or in terms of varying coenergy (which reaches a maximum at a rotor angle of 0°).

In this novel motor design, an arbitrary coil-shortening pattern may be achieved by wireless communication of commands that trigger the solid-state switches on the armature windings. In the normal (noninverted) configuration, the electronics that selectively short armature coils rotate along with the armature (rotor). When properly implemented, an adjustable commutation pattern may be used to dynamically control the motor's speed. Thus, this implementation can achieve variable speed without any modification to the source voltage.

C. Objectives

Although the principals of operation of all motor designs in use today were introduced more than 100 years ago [9], novel variations continue to emerge, primarily through control alternatives enabled by recent advances in power electronics and computer controls. The key to obtaining competitive ASD performance from this new type of design is to analyze the complex electromechanical dynamics in the space of possible switching patterns to optimize the implementation of an electronic control algorithm. Such optimization does not yield to steady-state analysis, since every switching change induces a new electrical transient (which are not synchronous with the line frequency). Appropriate analysis requires a time-domain model of the full

state dynamics of the system and detailed simulation of each candidate control algorithm.

In this paper, we present such a model [8], which takes advantage of SPICE-compatible software [10], [11], a conventional circuit analysis tool. SPICE allows the use of proven semiconductor models for accurate simulation of electric transients. Although traditionally a circuit simulation tool, SPICE has seen increasing use as a tool for merging semiconductor models with circuit analog models of mechanical [12], [13] and chemical systems [14].

In comparison to a prior model [6], [15], this work focused on the accuracy of its i - v models. Speed of the simulation is also an important consideration, since this model will be combined with potentially complex commutation circuits. To achieve these goals, the model was created by fitting data taken from a sample motor to a physically correct expression of the motor's electromagnetic properties and geometry. The resulting model is an accurate representation of the current experimental motor, yet flexible so future motors can be modeled by modifying parameter values.

Measurements of the voltage induced across the field and armature windings by a sinusoidal stimulus to a single armature winding were used to derive an expression for the mutual inductance from armature to armature and from armature to field as a function of angular position. Also the resistance and self-inductance of the armature and field windings, as well as coupling coefficients and eddy current losses (modeled as resistances) were measured. These measurements form the basis of the model.

II. ELECTROMAGNETIC MODEL

Voltages are induced across field and armature windings by dependent currents and coupling between the windings. The voltage across a field/armature winding x is given by

$$V_x = \left[L_x \frac{di_x(t)}{dt} + i_x(t) \frac{dL_x}{dt} \right] + \sum_{y \neq x} \left[M_{x,y}(\theta) \frac{di_y(t)}{dt} + i_y(t) \frac{dM_{x,y}(\theta)}{dt} \right] + R_x i_x(t). \quad (2.1)$$

Subscripts x and y refer to any of the nine components of the motor—the field winding and the eight armature windings. There are three key components in the equation (separated by brackets): the first resulting from the self-inductance of the field or armature windings, the second resulting from the mutual inductance between them, and the final term due to ohmic resistance. Preliminary characterization of the experimental motor demonstrated that the self-inductances (L) of the field and armature windings do not change significantly as a function of θ , and (dL/dt) terms were dropped from the model.

To make (2.1) conducive for implementation in the circuit model, two substitutions are made. With $v_{Ly} \equiv L_y(di_y/dt)$, the self-induced voltage, and $N_{x,y}(\theta) \equiv (M_{x,y}(\theta)/L_y)$, the effective turns ratio that couples armature winding x to armature winding y , $M_{x,y}(\theta)(di_y(t)/dt)$ becomes $N_{x,y}(\theta)v_{Ly}(t)$. Also, with L_y constant, $(dM_{x,y}(\theta)/dt)$ can be expressed as

Future models can use the same circuit model with new Fourier coefficients.

To avoid excessive data-acquisition requirements for our modeling, we chose to work with relatively coarse data sampling (every 11.5°) and reconstruct smooth waveform approximations from truncated Fourier sums. The choice for how many Fourier terms to preserve is a compromise. It is advantageous to use few terms, which results in faster computations in the simulator and less sensitivity to experimental errors (including inadequate subsampling of high spatial-frequency effects due to interactions between armature slots and field poles). However, enough terms must be retained to reconstruct the waveforms with sufficient accuracy that the slopes are also reasonably modeled, as the slopes contribute an important factor in predicting torque. Our modeling choice was to retain five significant Fourier components.

The technique employed to identify the magnitudes of the harmonic components was the discrete Fourier transform (DFT). Alternative curve-fitting approaches could be used, but this approach is particularly simple to implement. A DFT was computed with respect to the 32 data points acquired for each waveform, and only the chosen components (amplitude and phase shift) were preserved for reconstruction. We note that it should have been possible to model the waveforms using exclusively sine terms for the odd function and cosine terms for the even functions. By preserving the phase-shift information, our reconstructions do not have the expected symmetry, but they do better model the actual data. (The asymmetries are likely due to motor-specific variations, such as bearing eccentricity, lamination asymmetries, shaft curvature, and other irreproducible imperfections).

The present Fourier coefficients were developed from data taken from a sample motor with a $15.6\text{-V}_{\text{RMS}}$ 60-Hz stimulus applied to armature winding 1 with the field and all the other armature windings open circuited. Armature 1 was rotated in 11.25° increments covering 360° , while open-circuit rms voltages were recorded at each increment from the various windings. Referring to (2.2), it is apparent that such an experiment constrains

$$L_x \frac{di_x(t)}{dt}, \quad L_y \omega \frac{dN_{x,y}(\theta)}{d\theta} i_y(t), \quad \text{and} \quad R_x i_x(t)$$

terms to be zero. Therefore, discrete points of $N_{x,y}(\theta)$ are measured directly.

The DFT of the $N_{x,y}(\theta)$ data was taken, and coefficients and phase angles were extracted. The resulting five-harmonic expressions were found to produce a reasonable fit to the measured mutual inductance data. Because $M_{f,1}(\theta)$, $M_{2,1}(\theta)$, $M_{3,1}(\theta)$, $M_{4,1}(\theta)$, $M_{5,1}(\theta)$, and their corresponding $N_{x,y}(\theta)$ fully characterize the mutual inductance interactions, only these coefficients were computed. (Because armature 2 and armature 8 are equivalent, and the data for armature 8 were better behaved, coefficients for the 2–8 pair were extracted from armature 8’s data.) The actual data and reconstructed waveforms are shown in Fig. 3. The remaining curves $N_{2,1}(\theta)$, $N_{6,1}(\theta)$, $N_{7,1}(\theta)$ were generated simply by applying the appropriate phase shifts. The close fit between the simulations and the data indicates that our approximations for $M(\theta)$ are reasonable.

The coupling expressed in (2.2) by $N_{x,y}(\theta)v_{Ly}(t)$ (mutual inductance) changes as a function of angle as a result of the armature winding’s position with respect to the field. As is apparent from Fig. 1(c), an armature winding is under the field through only a portion of its rotation. The permittivity of the field iron is very high compared to air, thus, when two armatures have their axis of symmetry directly aligned with the field, their coupling is at its maximum. The field iron is wider than that of the armatures. For two armatures close together, there is a significant portion of their rotation for which both are completely under the field, resulting in a flattening of the mutual inductance peaks. Similarly, for two armature windings which are far apart, there is a significant part of their rotation where they are not both under a field pole, thus, their mutual inductance is relatively small. These trends are apparent in the measured data shown in Fig. 3.

The harmonics used to represent each waveform were thoughtfully chosen to ensure they would have a nonnegligible magnitude. It can be seen in Fig. 3 that the experimentally measured data (indicated by “+” signs on the graphs) for the field has half-wave symmetry and contains a single period of its waveform, as expected from the geometry of Fig. 1(c). This indicates that the first five odd harmonics (1, 3, 5, 7, and 9) will have the most significant amplitudes.

From the geometry, armature winding 8 should have even symmetry about $\pi/16$, and should be expressible by cosine harmonics of phase shift $n \cdot (\pi/16)$. However, when this phase was forced in the fit, poor results were obtained, particularly for higher harmonics. This is the result of slight asymmetries in the motor, described earlier. For this reason, phase was made an adjustable parameter, extracted for every Fourier component. For armature winding 8 (and 2), there are also two periods of the fundamental frequency in each revolution (and the collected data), thus even coefficients are used. There is no half-wave symmetry, thus the coefficients correspond to the 2nd, 4th, 6th, 8th, and 10th harmonics of the data. This argument also applies to armatures 3 (equivalent to 7) and 4 (equivalent to 6), thus the same harmonics of the data are used.

Finally, for armature 5, there are two periods of the fundamental frequency per revolution and half-wave symmetry in the data. This means that odd multiples of the 2nd harmonic should be used. Thus the harmonics used for armature 5 are the 2nd, 6th, 10th, 14th, 18th harmonics. Because there are 32 data points taken, the DFT produces a dc term and 16 harmonics. The 18th harmonic cannot be extracted, so only four harmonics were used in this case.

IV. VALIDATION TESTS

We first consider three simplified validation tests. In these tests, the state dynamics of the armature coil currents and field current were decoupled, limiting the differential equations to at most first order. Excitations were kept relatively low, staying within the magnetically linear region.

The model was first tested by simulating the conditions of data acquisition for mutual inductance. In these tests, the SPICE simulation was performed using the model with a 60-Hz $15.57\text{-V}_{\text{RMS}}$ sinusoidal voltage applied to armature coil 1 with

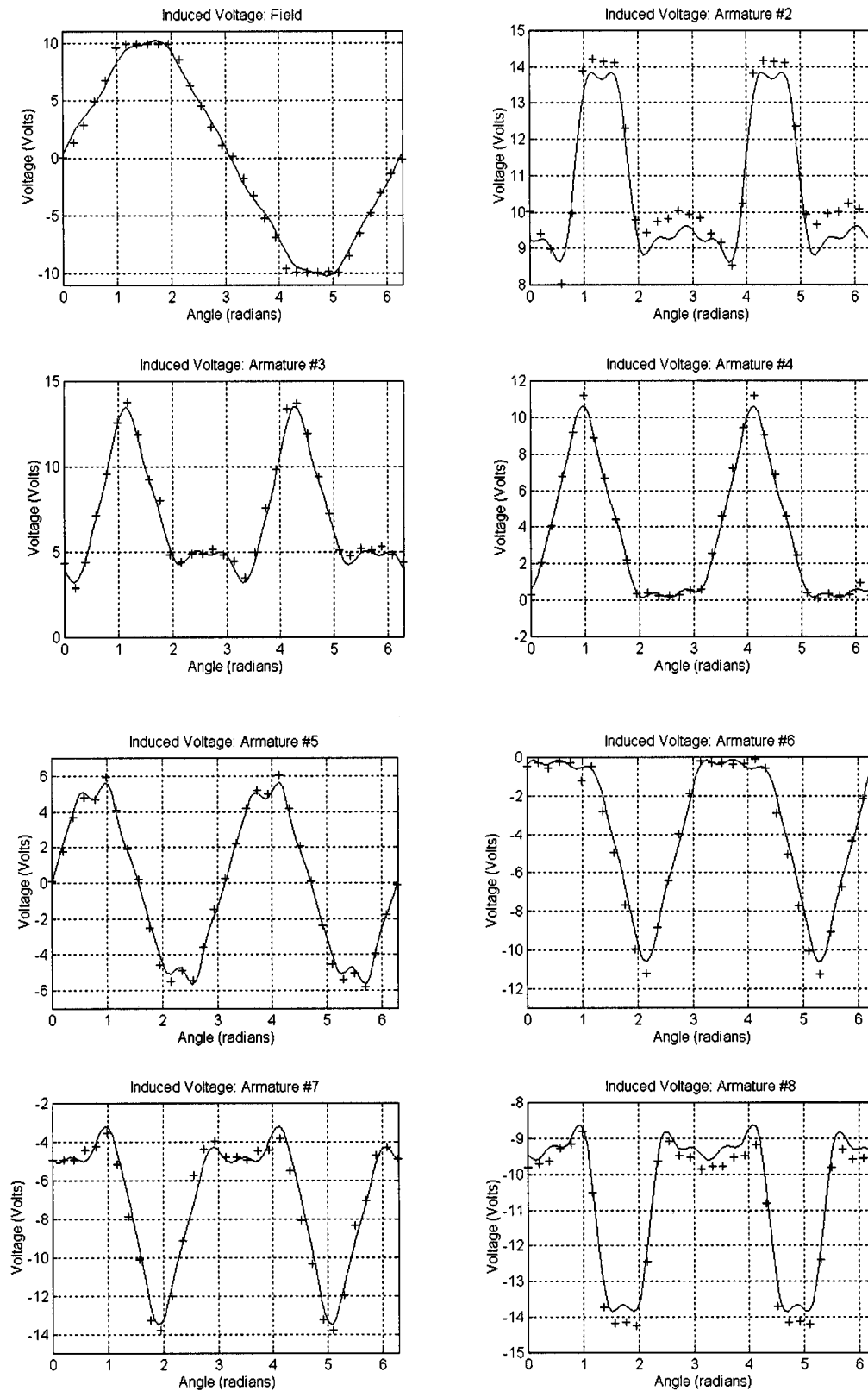


Fig. 3. Measured (“+”) mutual inductance and five-harmonic Fourier reconstruction with armature 1 driven by a $15.6\text{-V}_{\text{RMS}}$, 60-Hz sinusoid. The field and other armatures are open-circuited and induced rms voltages are measured and reconstructed.

all other coils open circuited. Mimicking the experimental conditions, this simulation simply reproduces the reconstructed waveforms shown in Fig. 3.

A second, more demanding test of the model is in the prediction of static torques. Under all conditions, whether transient or dc, torque is a function of coil currents and rotor angle. When

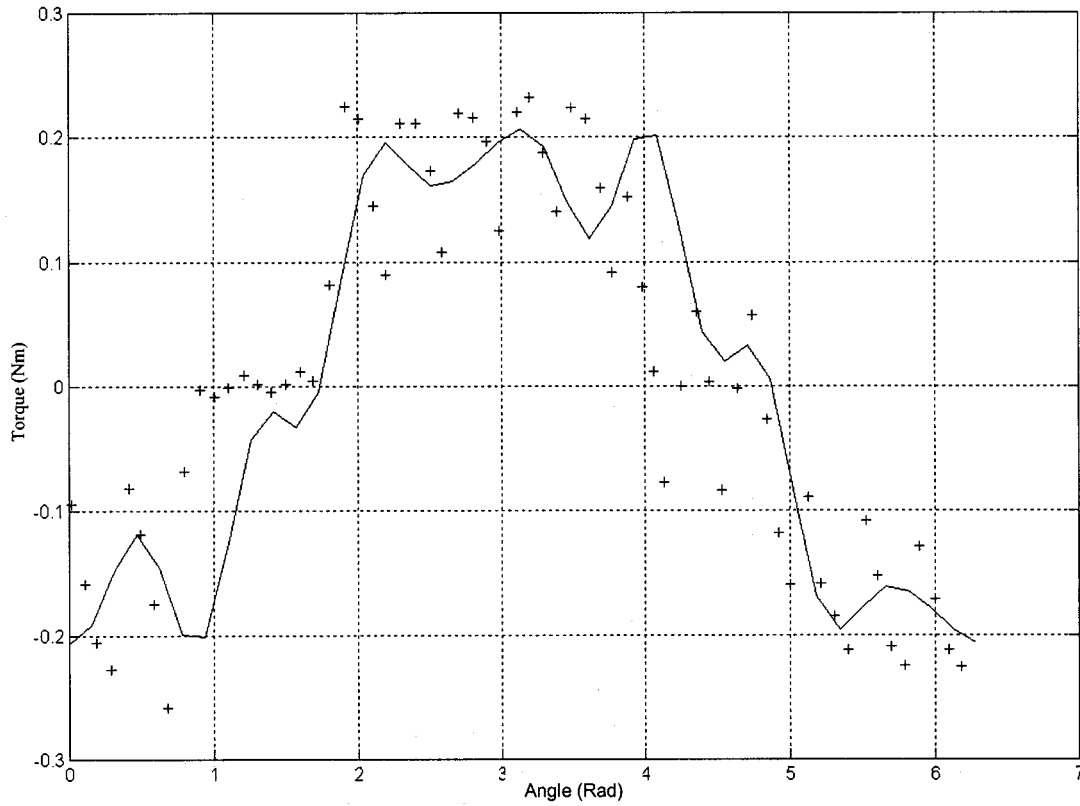


Fig. 4. Simulation and measured (“+”) motor test results of static torque with dc excitation. The x axis is in radians and the y axis is torque in newton meters.

the coil currents are a complex function of time, the resulting instantaneous torque production is also a complex function of time. To simulate the complex case, it is essential that we can first accurately predict torque production as a function of coil currents and rotor angle. By exciting both the field coil and one or more armature coils with dc currents, a steady torque is produced. Such static torque production is relatively easy to check against the simulation.

Since the model is linear, the torque produced may be computed with (2.3). For this test, a 3-A dc current was forced through both the field coil and armature coil 1. The resulting torque was measured as a function of angle using a reactionless torque meter. Measured data points are shown in Fig. 4, each marked with symbol “+.” The scatter is due to friction, including friction from the slip rings, motor bearings, and a toothed belt and pulleys coupling the rotating field housing to the torque meter. Since there are no electrical dynamics (dc currents are imposed), the self-inductance, mutual inductance, and back-EMF terms do not influence the simulation. This test is, therefore, a measure of the accuracy of the derivative of the mutual inductance model, $(dM_{f,1}/d\theta)$. For given armature and field currents, the peak torque production should occur at the maximum slope of $M_{f,1}(\theta)$, which occurs at the zero crossings of $M_{f,1}(\theta)$. Noting the slope of the field-to-armature mutual inductance, the expected shape of the static torque test produced in this experiment should have maximum value

$$\begin{aligned}\tau_{\max} &= 2 \cdot \frac{1}{2} I_f I_1 \frac{dM_{f1, \max}(\theta)}{d\theta} = (1)(3)(3)(25 \text{ mH/rad}) \\ &= 0.225 \text{ N} \cdot \text{m}.\end{aligned}$$

The torque prediction based on the slope of mutual inductance agrees favorably with the measured data, as shown in Fig. 4. In addition to friction noise in the data, effects with high spatial frequency are observed in the real motor, due to the interaction of slots in the armature with the field poles. Our lower order Fourier approximation does not include such higher frequency effects. However, this modeling imprecision is within the uncertainty due to friction. Noting that only the magnitude of the field-to-armature mutual inductance curve was approximated, it is a harsh test of this model to match the derivative of the approximated waveform to the derivative of the real mutual induction curve. We also note that the torque prediction capability of this model is limited to the magnetically linear region. Nonetheless, the success of matching mutual inductance derivatives via this linear-region torque test validates the mutual inductance modeling choices, including truncation of the Fourier representations to five terms.

Our third dynamically decoupled test focuses on back EMF. For this test, a 3-A dc current was forced in the field coil while all armature windings were open circuited. Since all current derivatives were zero, the influences of all self and mutual inductance terms were suppressed. Torques were also zero for this test, since torque production requires an interaction among multiple currents for this motor. However, back-EMF effects were excited by externally driving the motor at steady velocities. The voltage induced on armature winding 1 is

$$\nu_1 = \omega I_f \frac{dM_{1,f}}{d\theta}. \quad (2.4)$$

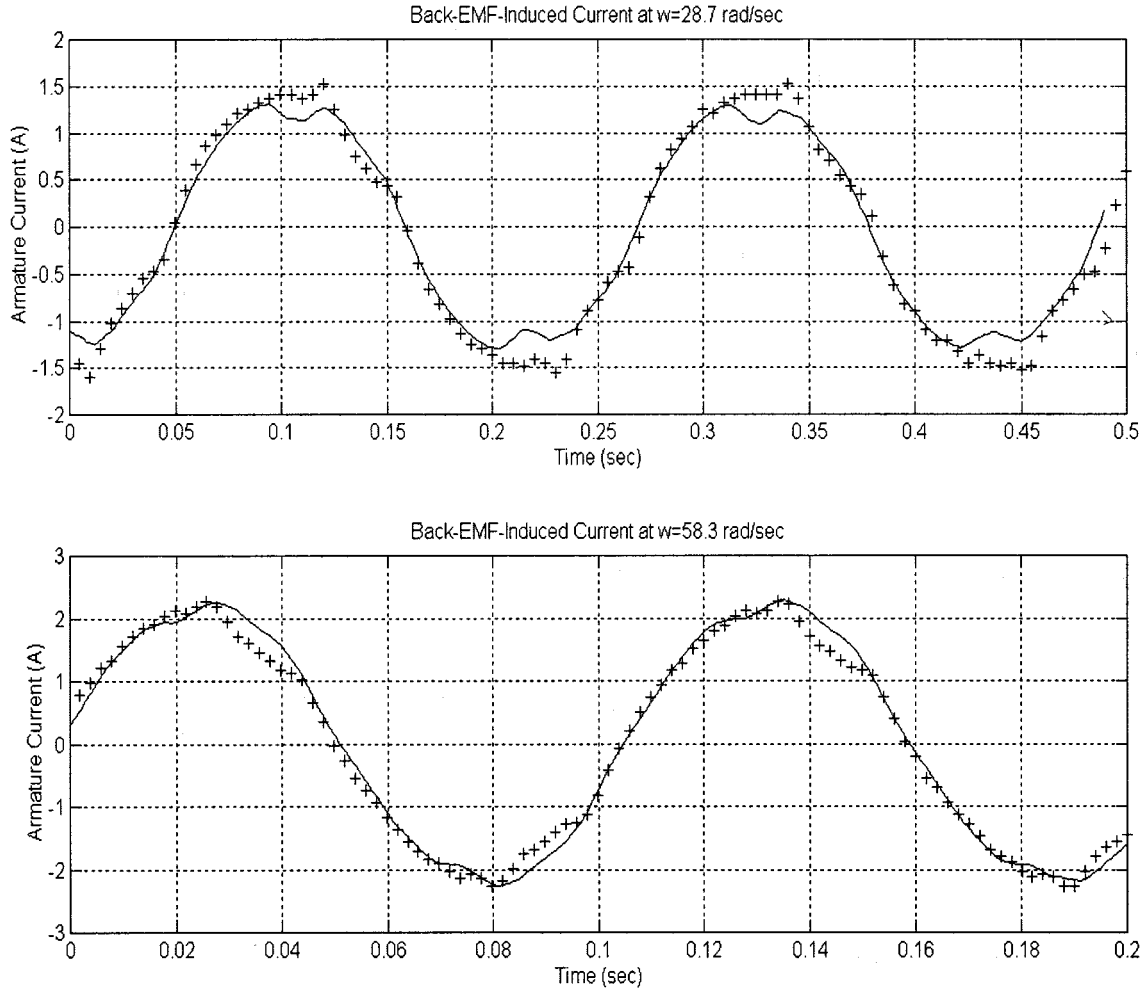


Fig. 5. Back-EMF-induced current in shorted armature 1 for two cases of rotational velocity, using series field windings. In both the test (“+”) and simulation, dc 1.85 A is applied to the field and a constant velocity (indicated on the plot) is imposed by an external servo motor. Armatures 2–8 are open circuit.

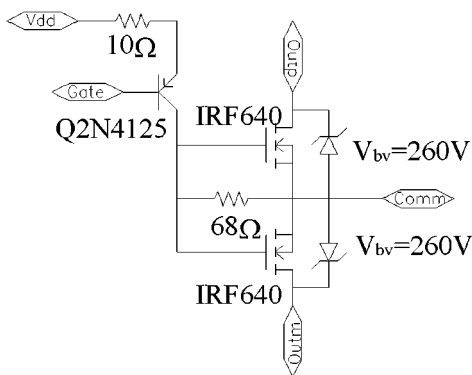


Fig. 6. Power MOSFET transistor switch used in commutation test. A 25-mA current pulse is used as gate signal to turn on the IRF640 switches.

RMS voltage should be a linear function of angular velocity (ω) with a slope equal to the field current multiplied by the rms mutual inductance. If M is assumed to be sinusoidal, then

$$v_{1, \text{RMS}} = \frac{\omega I_f M_{\text{peak}}}{\sqrt{2}} = \frac{(3 \text{ A}) \cdot (25 \text{ mH})}{\sqrt{2}} \omega = 53 \text{ mV} \cdot \omega. \quad (2.5)$$

Test results with the model produced a straight line with a slope of $49 \text{ mV} \cdot \omega$. Considering that this test depended on the slopes of our mutual-inductance function approximation, the agreement is good.

Just as voltage can be induced across a rotating, open-circuited armature through mutual inductance with the field, current can be induced into a shorted armature. A validation of the model under such a short-circuit test (with current levels kept below saturation) may be achieved through testing back EMF. The graphs in Fig. 5 show simulated and measured data of back-EMF-induced currents with the field biased at 1.85 A dc (below saturation levels) and the motor rotating at two different velocities. These particular tests were done using the inverted motor with the field connected in series, instead of in parallel, as in previous tests. This has the effect of multiplying the field resistance and inductance by four and the mutual inductance between the field and the armatures by two. These model parameters were adjusted accordingly, but other parameters were unchanged. Thus, the results of this test also verify the consistency of the model for series and parallel field windings. From these tests, we conclude that our model enables usefully accurate SPICE simulations of the DynaMotor in the linear magnetic region.

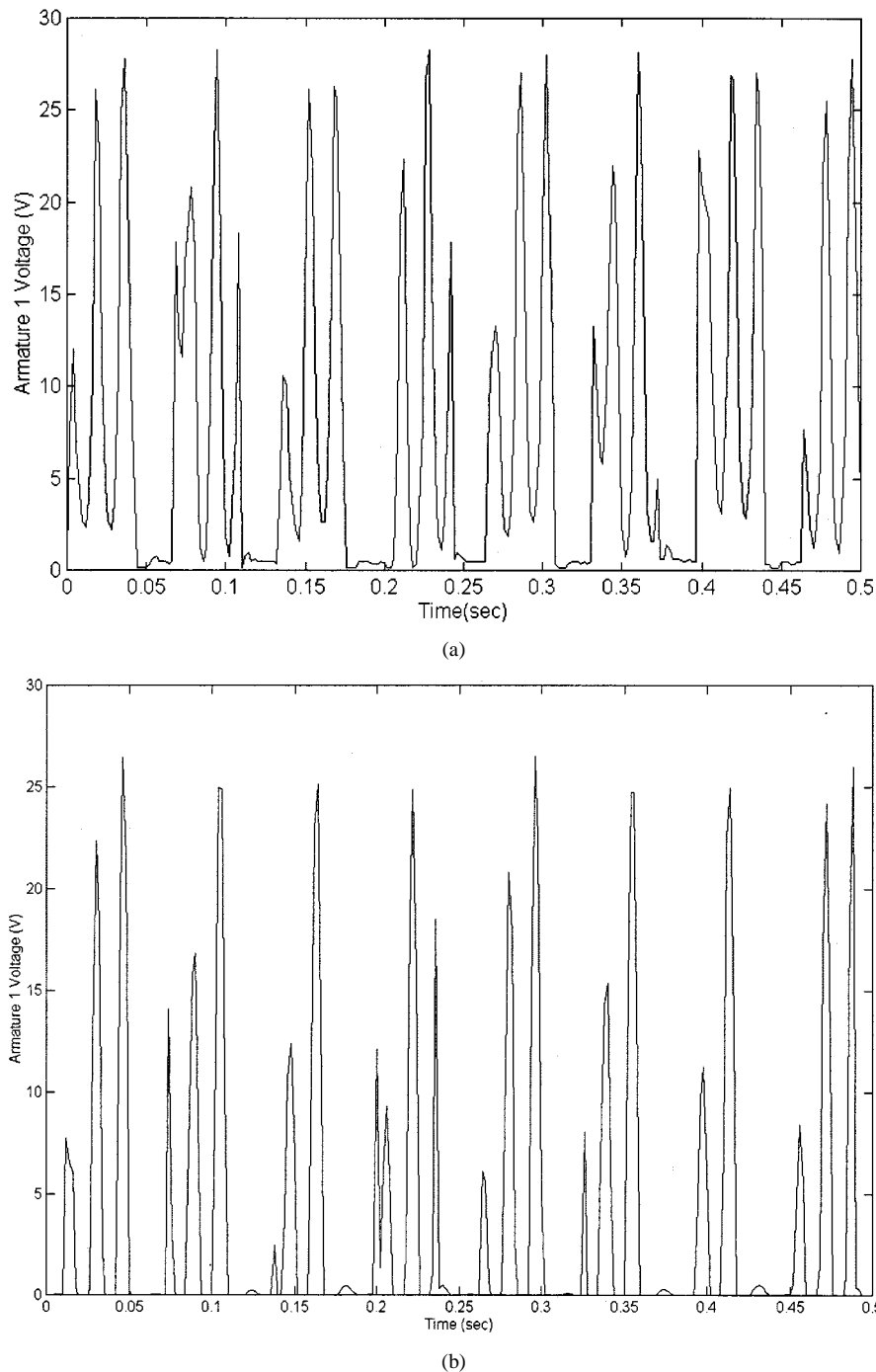


Fig. 7. (a) Switching transients from the inverted motor. In this test, the motor is forced to spin at 50 rad/s, with a field voltage of 27.6 V_{RMS} and a single armature switched on at -65° , off at 0° , on at 115° , and off at 180° . The oscilloscope collects a data point every 2 ms. (b) Switching transients from SPICE simulation. In this test, the motor is forced to spin at 50 rad/s, with a field voltage of 27.6 V_{RMS}, and a single armature is switched on at -65° , off at 0° , on at 115° , and off at 180° , as in the simulation above. This simulation is run with a maximum time step of 10 μ s and a print step of 2 ms.

V. TRANSIENT ANALYSIS WITH POWER MOSFET SWITCHES

The tests described in Section IV verified the uncommutated, open-circuit, and closed-circuit behavior of the model. In this section, dynamic tests including commutation are performed to examine the combined electromagnetic motor model with a mixed behavioral/transistor-level model of commutation circuitry. In principle, any switch, including a MOSFET, insulated gate bipolar transistor (IGBT), SCR, or TRIAC-based switch, could be simulated providing it has a

SPICE model. Power MOSFET switches permit the most flexibility in commutation, and these tests were performed using the IRF40 with the circuit shown in Fig. 6. The ends of an armature coil are connected to the terminals labeled “Outp” and “Outm” in this figure. The commutation model uses the rotor angle as an input and applies the appropriate gate signals to the switches to achieve specified commutation and overlap angles.

Tests were performed using both the “inverted motor” and the simulation model. A computer-controlled servo motor was

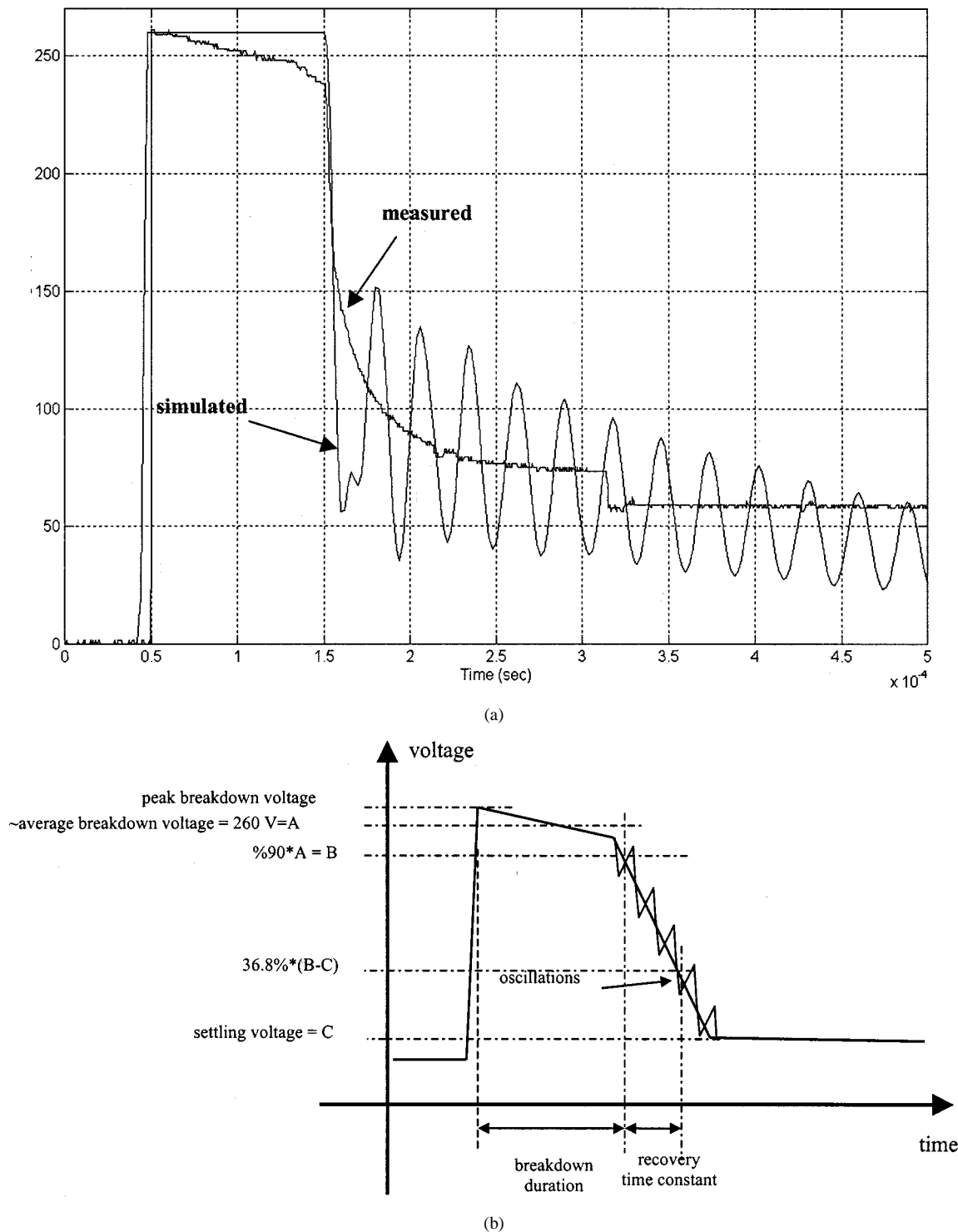


Fig. 8. (a) Real and simulated breakdown waveforms for a test with 27.6-V_{RMS} field voltage, 49° commutation angle, and no overlap at a rotational velocity of 50 rad/s. (b) Breakdown metrics defined.

attached to the inverted motor, forcing it to spin at a constant 50 rad/s. A 27.6-V_{RMS} 60-Hz voltage was applied to the field, and a single armature winding of the inverted motor was turned on at -65° , off at 0° , on at 115° and off at 180° , as measured by a resolver internal to the servo motor. The voltage across the commutated armature was measured, while the rest of the armatures remained open circuited in this test. The same test was performed using the simulation model.

In Fig. 7(a) and (b), transient behavior over 0.5 s is shown for these two identical tests. At 50 rad/s, there should be eight switching events in 0.5 s, which is demonstrated in both figures. There are 30 60-Hz cycles in 0.5 s, but those that occur during commutation are masked, so ~ 23 are observed. Both figures also show similar periodicity and shape. In both cases, there are eight clusters of three pulses, separated by periods of near-zero voltage when the armature

TABLE I

COMPARISON OF BREAKDOWN METRICS FOR MEASURED DATA AND SIMULATION FOR 27.6-V_{RMS} FIELD VOLTAGE, 49° COMMUTATION ANGLE, AND NO OVERLAP AT A ROTATIONAL VELOCITY OF 50 rad/s. *IN BOTH MEASUREMENT (0.5-μs SAMPLE RATE) AND SIMULATION (2-μs SAMPLE RATE), THIS METRIC IS VERY CLOSE TO THE RESOLUTION LIMIT OF THE TEST

	Average breakdown duration (μsec)	Average recovery time constant (μsec)	Average field voltage phase for breakdown (degrees)	Peak Breakdown Voltage (V)	Time to Breakdown* (μsec)
Measured	119.5	75.8	47.7	262	0.9
Simulation	129.4	64.0	42.7	260	2.2
Difference	8.3%	15.6%	4.5%	0.8%	-

winding is shorted. The first pulse is a combination of the voltage induced during a switch off, the inductively coupled field voltage, and the back EMF. The remaining two pulses are the 60-Hz field voltage and back EMF.

Some of these cases result in very short high-voltage transients, but the sampling rate is too small to show up on the oscilloscope or in simulation. For tests with the inverted motor, the sampling rate is set by the time scale of the digital oscilloscope used to view the waveform. For the simulator, the internal time step sets the sampling rate, and is determined by the simulator itself, although a maximum time step may be set. This data is then downsampled by the printing step size, which may be set as desired. In this test the print step was set to 2 ms to be comparable with data collected from the oscilloscope. More accuracy may be achieved with a smaller maximum time step and print step at the expense of greater simulation time. In this test, a typical breakdown event lasts $\sim 100 \mu\text{s}$, and cannot be seen on an oscilloscope without a time scale significantly reduced from the one that produced Fig. 7(b). Similarly, it cannot be seen in simulation without a greatly reduced maximum time step.

The high-voltage transients are the result of armature inductance and are limited by reverse breakdown of the MOSFETs in this circuit. When a switch is turned off, the interrupted current causes a large voltage to develop across the armature terminals. If the voltage exceeds the reverse breakdown voltage of the substrate diode in the power MOSFET, the diode will conduct and clamp the voltage. The diode will remain conducting until sufficient energy is dissipated so that its voltage drops below the breakdown voltage. Fig. 8(a) shows examples of typical real and simulated breakdown waveforms. In this test, the motor is spun at a constant speed of 50 rad/s, the commutation center angle is set to -49° , and there is no overlap between consecutive armatures.

A variety of switching behaviors were observed in the real motor: nonbreakdown events, breakdown events of varying duration, and oscillating breakdown events. In the model, similar breakdown and nonbreakdown events occur. In simulation, oscillations at 36 kHz always occur on the recovery of a breakdown. For the actual inverted motor the oscillations are infrequent. Measured oscillations for the inverted motor have a typical frequency of 85 kHz and occur during the breakdown and recovery period.

The discrepancy in oscillating behavior is not well understood. It is hypothesized that the oscillations that occur in simulation are damped by parasitics of the real motor that are not modeled. Also, oscillations that occur for the inverted motor may be due to an occasional loss of contact with the slip rings that power the field during rotation. In such an instance, the energy built up in the armature cannot be transferred to the field, and thus the oscillations are not damped. Additionally, the loss of contact would mean the armature has a different reflected impedance, which could explain the difference in frequency of the oscillations.

Aside from the oscillating behavior, agreement between simulation and test results are good. Breakdown transients from simulation and real data were collected and analyzed using metrics defined in Fig. 8(b). The results are summarized in Table I.

VI. CONCLUSIONS

A modular circuit model was developed that is easily adaptable to other N -coil single-phase brushless ac motors and conveniently interfaces to test switching circuits. The model is based on Fourier expansions of measured mutual inductance interactions between different combinations of the field and armature windings, and measurements of the coil resistance and inductance. In addition, a model to emulate potential commutation algorithms with realistic semiconductor switching circuits has been developed and can be interfaced with the model of the motor.

The model is able to accurately predict current and voltage characteristics as well as estimate torque, both statically, and dynamically when interfaced with the commutation model. The model has been demonstrated to agree with electrical tests of an inverted motor on a large time scale, and has also given reliable predictions of small time-scale details. Of particular interest in this application was its ability to predict the behavior of power MOSFET switches during an event where the transistors' substrate diodes are turned on as a result of the high voltages generated across the switch after a command to open circuit. Data were collected and analyzed for commutation tests performed on an inverted brushless motor. Metrics were compared to data collected from simulation with good agreement. The model is a useful tool, which will be used to examine current and voltage

waveforms when operated with a variety of potential switching circuits and speed control algorithms.

REFERENCES

- [1] S. Yamamura, *AC Motors for High-Performance Applications: Analysis and Control*. New York: Marcel Dekker, 1986.
- [2] J. C. Andreas, *Energy-Efficient Electric Motors: Selection and Application*, 2nd ed. New York: Marcel Dekker, 1992.
- [3] V. Subrahmanyam, *Electric Drives: Concepts and Applications*. New York: McGraw-Hill, 1996.
- [4] L. Haner, "Repulsion motor," U.S. Patent 5 491 398, Feb. 13, 1996.
- [5] —, "Repulsion motor," U.S. Patent 5 424 625, June 13, 1995.
- [6] W. Newman, I. Risch, Y. Zhang, S. Garverick, and M. Inerfield, "Analysis, design and control of a novel, optically-commutated adjustable-speed motor," *Proc. SPIE-Sensors Contr. Intell. Machining, Agile Manuf., Mechatron.*, vol. 3518, pp. 200–207, Nov. 1998.
- [7] A. E. Fitzgerald, C. Kingsley Jr., and S. D. Umans, *Electric Machinery*, 5th ed. New York: McGraw-Hill, 1990.
- [8] M. Inerfield, "Commutation control circuitry for a brushless AC motor," M.S. thesis, Dep. Elect. Eng. Comput. Sci., Case Western Reserve Univ., Cleveland, OH, Jan. 1999.
- [9] B. Bowers, "The early history of the electric motor," *Philips Tech. Rev.*, vol. 35, no. 4, pp. 77–95, 1975.
- [10] A. Vladimirescu, *The Spice Book*. New York: Wiley, 1994.
- [11] *The Design Center: Circuit Analysis—Reference Manual*, Microsim Corporation, Irvine, CA, 1993.
- [12] A. A. Fardoun, E. F. Fuchs, and H. Huang, "Modeling and simulation of an electronically commutated permanent-magnet machine drive system using SPICE," *IEEE Trans. Ind. Applicat.*, vol. 30, pp. 927–937, July/Aug. 1994.
- [13] J. Faiz and A. Keyhani, "PSPICE simulation of single-phase induction motors," *IEEE Trans. Energy Conversion*, vol. 14, pp. 86–92, Mar. 1999.
- [14] T.-F. Wu, J.-C. Hung, and T.-H. Yu, "A PSpice circuit model for low-pressure gaseous discharge lamps operating at high frequency," *IEEE Trans. Ind. Electron.*, vol. 44, pp. 428–431, June 1997.
- [15] I. P. Risch, "Simulation development for design and control of a novel single-phase, brushless motor," M.S. thesis, Dep. Elect. Eng. Comput. Sci., Case Western Reserve Univ., Cleveland, OH, Aug. 1998.



Michael A. Inerfield (S'96) received the B.E. degree in electrical engineering in 1996 from The Cooper Union for the Advancement of Science and Art, New York, NY, and the M.S. degree in electrical engineering in 1999 from Case Western Reserve University, Cleveland, OH, where he is currently working toward the Ph.D. degree.

He is also currently a Research Assistant at Case Western Reserve University.

Mr. Inerfield received a First Place Award in the IEEE Region I Student Paper Contest in 1996.



Steven L. Garverick (S'84–M'85–SM'94) was born in Shelby, OH, in 1957. He received the B.S., M.S., E.E., and Ph.D. degrees in electrical engineering from Massachusetts Institute of Technology, Cambridge, in 1979, 1980, 1984, and 1987, respectively.

From 1980 to 1983, he was a Member of the Research Staff at the M.I.T. Lincoln Laboratory, where he worked on the development of wafer-scale VLSI systems. In 1986, he joined the Research Staff of the General Electric Company, Corporate

Research and Development, where he developed data acquisition and digital signal processing electronics for the measurement and distribution of electrical power, medical imaging systems, and aircraft engine control. In 1992, he joined the faculty of Case Western Reserve University, Cleveland, OH, where he is currently an Associate Professor in the Department of Electrical Engineering and Computer Science. His interest in integrated circuit design and technology for analog and mixed-signal applications is presently directed toward transducer interface and communication circuits for applications including micromotor control, smart structural materials, wireless SiC microsensors, autonomous microrobots, and three-dimensional ultrasonic imaging. He has authored 35 papers published in refereed journals and conference proceedings and is the holder of 15 U.S. patents.

Dr. Garverick is a member of Tau Beta Pi, Eta Kappa Nu, Society for Automotive/Aerospace Engineers, and American Society of Engineering Educators. He was the recipient of the Case Western Reserve University Award for Distinguished Graduate Teaching.



Wyatt S. Newman (M'87) received the S.B. degree in engineering science from Harvard College, Cambridge, MA, the S.M. degree in mechanical engineering in thermal and fluid sciences from Massachusetts Institute of Technology, Cambridge, the M.S.E.E. degree in control theory and network theory from Columbia University, New York, NY, and the Ph.D. degree in mechanical engineering in design and control from Massachusetts Institute of Technology in 1978, 1980, 1982, and 1988, respectively.

He is currently a Professor in the Department of Electrical Engineering and Computer Science, Case Western Reserve University, Cleveland, OH. His research is in the area of mechatronics, in which he is the holder of eight patents and the author of more than 80 technical publications. Between 1980–1988, he was a Senior Member of the Research Staff at Philips Laboratories, where he was engaged in electromechanical design and control. His current research includes projects in robotics, rapid prototyping, and motor design and control.

Prof. Newman was named a National Science Foundation Young Investigator in 1992.



Yuandao Zhang received the B.S. degree from Shanghai Jiaotong University, Shanghai, China, in 1965.

From 1965 to 1990, he was a Senior Engineer with Tianjin Instrument Research, China, where he worked on control systems for navigational equipment. In 1990, he joined the Technical Staff of the Center for Automation and Intelligent Systems Research, Case Western Reserve University, Cleveland, OH.